From Performance Measurements to Molecular Level Characterization: Exploring the Differences between Ultraviolet and Damp Heat Weathering of Photovoltaics Modules

Robert Heidrich, Nikola Babic, Oscar Lacroix-andrivet, Charles-emmanuel Dutoit, Camille Bainier, Anton Mordvinkin, Ralph Gottschalg, Herve Vezin, Carlos Afonso, Simon Pondaven

From Performance Measurements to Molecular Level Characterization: Exploring the Differences between Ultraviolet and Damp Heat Weathering of Photovoltaics Modules

Robert Heidrich,* Nikola Babić,* Oscar Lacroix-Andrivet, Charles-Emmanuel Dutoit, Camille Bainier, Anton Mordvinkin, Ralph Gottschalg, Hervé Vezin, Carlos Afonso, and Simon Pondaven

The degradation behaviors of the encapsulant and the imbedded additives significantly determine the reliability of solar modules. Nevertheless, a link between the degradation of the encapsulant, including the additive interactions, and the longevity of the overall module is rarely established until now. Herein, mini-modules containing ethylene-vinyl acetate copolymer (EVA) as encapsulant are subject to damp heat (DH) or ultraviolet (UV) weathering based on IEC 61215. Macroscopically, the degradation under both weathering types characterized by I–V measurements and electroluminescence (EL) measurements is diverging in dependence on the used stressor. Using electron paramagnetic resonance and orbitrap mass spectrometry, it is shown that deacetylation of the EVA occurs significantly for both types of weathering. In the case of DH, however, the mechanism of action of the UV stabilizer is hindered, so that strong encapsulant degradation is observed despite a lower energy input in comparison with UV. Furthermore, the produced acetic acid under DH weathering leads to the observed reduction in EL, an increase in series resistance, and, a reduction of the performance of the modules. The work carried out shows that the degradation of the solar modules is strongly dependent on the behavior of the UV stabilizer.

1. Introduction

Today, the increase in global energy demand as well as the need to reduce CO_2 emissions is driving the development of renewable energies, especially solar photovoltaics (PV). Since 2010, solar PV has shown an impressive learning curve and is now a mainstream energy source, which is the result of consistent cost reduction and technical performance improvements.[1] However, PV modules installed in the field are facing various climatic conditions: humidity, temperature cycling, ultraviolet (UV) exposure, mechanical stress, etc. that could be combined at very different intensity levels, leading to various degradation and failure scenarios.[2–5] With a mass share of ≈6.5%, polymer materials (encapsulants and backsheets) only make up a small proportion of a solar module.[6] Nevertheless, a large number of module defects can be attributed to the failure of polymer components.[7] Furthermore, the interaction of different polymer layers within a module can have a major influence on its degradation behavior.[4,8–10] Understanding diverse degradation modes

R. Heidrich, A. Mordvinkin, R. Gottschalg
Fraunhofer CSP
Otto-Eissfeldt-Strasse 12, 06120 Halle (Saale), Germany
E-mail: robert.heidrich@csp.fraunhofer.de

R. Heidrich, R. Gottschalg
Anhalt University of Applied Sciences
Bernburger Strasse 55, 06336 Koethen (Anhalt), Germany

The ORCID identification number(s) for the author(s) of this article can be found under https://doi.org/10.1002/solr.202400144.

N. Babić, O. Lacroix-Andrivet, S. Pondaven
TotalEnergies OneTech
Centre de Recherche de Solaize (CRES)
Chemin du canal, BP 22, 69360 Solaize, France
E-mail: nikola.babic@totalenergies.com

N. Babić, C.-E. Dutoit, H. Vezin, S. Pondaven
Joint Laboratory—CR2ME: Centre de Résonance Magnétique Électronique pour les Matériaux et l' Énergie
59655 Villeneuve d'Ascq, France

O. Lacroix-Andrivet, C. Afonso
International Joint Laboratory—iC2MC: Complex Matrices Molecular Characterization
TRTG
BP 27, 76700 Harfleur, France

affecting PV modules, particularly those involving polymer materials, becomes imperative, enabling informed component selection and accurate quantification of performance losses. Surprisingly, there are only a few studies to date that correlate the degradation of polymer layers with the macroscopic degradation of a solar module (i.e., deterioration of electrical parameters).[9,11,12]

Solar modules are designed to last at least 25 years, although it has been shown in the past that this is only economical if an annual degradation rate of 0.73% is not exceeded.[13] However, depending on climatic conditions and material combinations in PV modules, annual degradation rates of well over 1% are possible, and earlier total failures can be expected at any time.[14,15] For these reasons, it is essential to test the modules thoroughly before using them in the field. Even though with IEC 62788-7-2, there is now a standard for testing polymer components,[16] the complete module is tested under the conditions defined in IEC 61215.[17] Typically, damp Heat (DH) and UV tests are carried out according to IEC 61215.[17] There are many studies that deal with the degradation of individual components of the solar module (e.g., cell degradation or degradation of polymer layers) as a function of the two types of weathering, however, an integral approach to understand the degradation of the complete module is often missing.[18–22]

Although new types of modules sometimes use polyolefin-based elastomers or thermoplastic polyolefins, ethylene-vinyl acetate copolymer (EVA) has been the main encapsulant used so far.[23,24] To date, the effects of these tests on the encapsulation material and, in this context, on the reliability of the overall module are not fully understood. The degradation of EVA is a complex process with various intermediate reactions, which can proceed differently depending on the external conditions.[15,24–27] In addition, the degradation of EVA is influenced by the additives contained in the encapsulant, whereby UV additives and antioxidants in particular are intended to protect the polymer.[28,29]

The given study is intended to close the abovementioned knowledge gaps. To achieve this goal, a combination of different analytical methods is used, ranging from macroscopic performance characteristics of the overall modules by electrical characterization and electroluminescence (EL) measurements to molecular analysis of the encapsulant by electron paramagnetic resonance measurements (EPR) and Orbitrap mass spectrometry (MS). Hindered amine light stabilizers (HALS) have a catalytic

C.-E. Dutoit, H. Vezin
Laboratoire Avancé de Spectroscopie pour les Interactions
la Réactivité et l'Environnement (LASIRE)
Université Lille Nord de France
CNRS UMR8516
59655 Villeneuve d'Ascq, France

C. Bainier
TotalEnergies OneTech
R&D Power
7-9 Boulevard Thomas Gobert, 91120 Palaiseau, France

C. Afonso
Normandie Univ., COBRA, UMR6014 and FR3038
Université de Rouen
INSA de Rouen
CNRS, IRCOF
1 rue Tesnière, 76821 Mont-Saint-Aignan Cedex, France

mechanism of action and one of their active intermediates is stable radicals called nitroxides. Being the analytic technique of choice for studying radicals, EPR is used to investigate the antioxidant activity of HALS under different weathering conditions. Concerning Orbitrap MS, it corresponds to a Fourier transform mass spectrometry (FTMS) technique suited for the characterization of complex matrices thanks to its high sensitivity, high mass accuracy, and very high resolution. It allowed us to characterize the HALS additive and the various forms of degradation of the base polymer at the molecular level. The combination of these different techniques provides a better understanding of encapsulant aging by linking performance test results to molecular markers.

2. Methodology

2.1. Sample Design

The used one-cell mini-modules correspond to the conventional structure of a solar module. The substrate was 3 mm float glass. The EVA has an UV cutoff (5% transmittance at 350 nm), a vinyl acetate content of 26–28%, and a thickness of 0.4–0.6 mm. A Meier ICOLAM 10/08 was used for lamination with the following parameters: the laminator was preheated to 55 °C. The samples were then placed in the laminator, which was evacuated for 6.5 min and heated to 80 °C. The modules were then pressed with 600 mbar and heated to 155 °C within 3 min. The temperature and pressure were maintained for a further 15 min. Finally, the laminator was cooled down to 55 °C within 30 min, whereby the 600 mbar pressure was kept constant.

The gel content after lamination is reported to be over 85% by the datasheet, while measurements of separate films show gel contents of ≈90%. Thus, no remaining crosslinking peroxides are expected. The EVA has a reported transmittance of over 91% and was used as front and back encapsulant. Solar cells were based on PERC technology with 5 busbars and 4 electrical contacts for I–V measurements. The backsheet is based on polyethylene terephthalate with a thickness of 320 μm. The moisture transmission rate of the backsheet is reported to be 1.9 g m^{-2} per day. After lamination, the edges of the mini-modules were sealed with an aluminum tape to simulate a frame and make it more difficult for moisture to penetrate.

The encapsulation material used was initially characterized by pyrolysis gas chromatography-mass spectrometry (PY-GCMS) for investigating the additive composition. The PY-GCMS setup has been described in detail in one of our previous publications.[30] However, in this work only a qualitative additive analysis was executed. **Table 1** lists the results of the additive analysis. A combination of crosslinking peroxide and crosslinking accelerator was used to enable the reported gel content after lamination. In addition, an adhesion promoter was admixed. For stabilization, a combination of an antioxidant, an UV absorber, and a HALS (UV stabilizer) was used.

2.2. Weathering

Two different types of weathering were performed for this study. UV weathering was conducted in CTS CSL-70/1500 climatic

Table 1. Results of the qualitative PY-GCMS analysis. Substances with ++ are certainly detected in significant amounts. For substances with +, only traces (small intensities) were found.

Name	Function	CAS	Amount
Luperox TBEC	Crosslinking peroxide	34443-12-4	++
TAIC	Crosslinking accelerator	1025-15-6	++
Silane A-174	Adhesion promoter	2530-85-0	+
BHT	Antioxidant	128-37-0	+
Cyasorb UV 531	UV absorber	1843-05-6	++
Tinuvin 770	HALS, UV stabilizer	52829-07-9	++

chambers. Here, the parameters were set to 60 °C chamber temperature, 5% relative humidity, and an integrated UV intensity of 175 ± 35 W m^{-2} (depending on the sample position in the chamber) between 300 and 400 nm. For example, lamp spectrum of the chamber and the intensity homogeneity of the lamps are displayed in the supporting information. The used parameters are in accordance with the UV preconditioning test MQT 10 of the IEC 61215-2.[17]

DH weathering was performed in a CTS CW + 40/8/8 chamber. The parameters were set to 85 °C chamber temperature and 85% relative humidity which are in accordance with the DH test MQT 13 of the IEC 61215-2.[17] The modules were characterized after 0, 500, 1000, 1500, and 2000 h, as described in **Table 2**. After the electrical characterization, 3 modules of every weathering step were removed for further analysis.

2.3. Characterization Methods

2.3.1. I–V Characterization and EL Measurements

The I–V characteristics were recorded using a Berger Lichttechnik solar simulator (flasher system). The tests were performed at 25 °C with 1000 W m^{-2} irradiated intensity (standard test conditions). The flasher corresponds to class A in the categories of homogeneity, spectral match, and temporal stability. The repeatability is less than 0.3% deviation. The flasher was calibrated with a reference module before each measurement series.

EL measurements were performed with a great eyes LumiSolar Professional system. A cooled GE2048 512 BI MID

Table 2. Sample list.

Aging type	Aging duration [h]	UV dose [kWh m^{-1}]
Native mini-module	0	0
Mini-modules aged under UV irradiation	UV-500	87.5
	UV-1000	175.0
	UV-2000	350.0
Mini-modules aged under DH	DH-500	0
	DH-1000	0
	DH-1500	0
	DH-2000	0

CCD sensor is installed in the camera. For the EL measurements, the modules were powered with 8.5 A.

2.3.2. EPR Measurements

Sample Preparation and EPR Spectroscopy: EVA was sampled using scalpel by cutting out rectangles (2.5×20 mm) of the entire stack except the glass (backsheet, front and back layer of EVA, and solar cells). The samples were taken from two spots for each mini-module: the center of the mini-module, and the edge of the mini-module (the edge sample contained only the two layers of EVA and backsheet). Samples were placed in 5 mm quartz EPR tubes and EPR spectra were recorded at room temperature using a Bruker EMXnano EPR spectrometer (Bruker, Wissembourg, France) operating at X-band (9.61 GHz) with the following parameters: modulation frequency, 100 kHz; modulation amplitude 4.0 G; time constant, 20.48 ms; conversion time, 60.00 ms; center field, 3425.45 G; sweep width, 300 G; sweep time 45.0 s; microwave power, 10 mW; number of scans, 10; Pts/Mod. Amp, 10.00; and resolution 750 points. Data acquisition and processing were performed using Bruker Xenon software. The amount of nitroxide present in the sample is directly proportional to its EPR signal intensity. Since a similar spectral appearance of nitroxide was observed in all samples, the intensity was measured as the height of the central line and was normalized by the mass of the sample. For the shown set of samples, one sample per condition per time point was analyzed. Relative measurement error was calculated from three repetitions of 500 h UV sample and was found to be ±16%. It was used for other samples as a generic relative error.

Sample Preparation and EPR Imaging: Samples were prepared by cutting a rectangle (5.0×20 mm) of the entire solar mini-module (including the glass support). EPR imaging measurements were carried out on a conventional X-band Bruker ELEXSYS E580 spectrometer operating at about 9.5 GHz and room temperature. The microwave power and the modulation amplitude used were set to 5 mW and 10 G, respectively. The samples were placed into the magnet equipped with ZY two-axis field gradients. A gradient strength of 100 G cm^{-1} and a field-of-view of 20 and 15 mm have been used to record spatial–spatial and spectral–spatial images, respectively. Both images were performed using 402 projections and a size of 512×512 pixels corresponding to a pixel size of 0.0391 mm (0.0293 mm). The final images were reconstructed after a deconvolution of the recorded projections under a magnetic field gradient from a spectrum with field gradients turned off. Subsequently, a filtered back projection using the Fourier transform was applied. EPR images analysis and spectral simulations were done with the EasySpin package for MATLAB.[31]

2.3.3. Orbitrap MS Measurements

Sample Preparation Prior to MS Analyses: EVA pieces were sampled from the edge of the mini-modules using a scalpel. 1 mL of heptane for each 30 mg of EVA was placed in a glass vial. To solubilize a part of the EVA, the vials were treated for 1 h in an ultrasonic bath. The resulting solutions were then centrifuged at 4000 rpm for 5 min. Supernatants were then

collected to be analyzed by direct infusion on the Orbitrap instrument. A scheme of this procedure is displayed in Figure S1, Supporting Information.

MS Analyses: Orbitrap MS analyses were carried out using a Thermo Orbitrap QExactive Plus equipped with a commercially available atmospheric pressure chemical ionization (APCI) source. The instrument was calibrated before the analyses using the Thermo Scientific Pierce LTQ ESI positive ion calibration solution. Mass spectra were obtained on a mass range between m/z 100 and 1200 with an analysis duration of 6 min at 1 Hz resulting in 280 k resolution at m/z 200. The automated gain control target was set at 10^6, and the maximum injection time at 50. S-Lens RF was set at 100 to have a better sensitivity toward a high mass range. Indeed, this lens allows a 10-fold increase in the ion transfer efficiency in the MS/MS mode, and a threefold to fivefold increase for the full scan analysis. For the ionization source, a sheath gas and an auxiliary gas were set at 20 (a.u) and 10 (a.u), respectively, corona discharge was set at 4.5 μA, and the source temperature was 300 °C. MS data were treated using FreeStyle 1.6 software. Molecular formulae were attributed to each signal using a heteroatom tolerance set at a maximum of 2 nitrogen atoms and 10 oxygen atoms, with an error tolerance set at 2 ppm. Molecular maps and heteroatom class distribution were plotted using PyC2MC[32] and OriginPro softwares.

For the Kendrick mass defect (KMD) plots, KMD of molecules were calculated using the classical CH_2 base unit to obtain the Kendrick masses (KMs) using the following equations:

$$KM = \text{observed IUPAC mass}$$
$$\times \frac{\text{nominal mass of CH2 (14)}}{\text{IUPAC mass of CH2 (14.01565)}} \quad (1)$$

$$\text{Nominal KMaNKM} = \text{round}(KM) \quad (2)$$

$$\text{KM defect aKMD} = \text{aNKM–KM} \quad (3)$$

The nominal KM corresponds to the KM rounded to the nearest integer.

3. Results and Discussion

3.1. Electrical Characterization

To investigate the macroscopic degradation behavior of the modules, an electrical characterization was carried out for both types of weathering in 500 h steps. The behavior of the characteristic parameters: short circuit current I_{SC}, maximum power output P_{max}, open circuit voltage V_{OC}, fill factor FF, series resistance R_S, and efficiency η is discussed. The electrical characterization of the weathered mini-modules is displayed in **Figure 1**. Changes in the I_{SC}, P_{max}, V_{OC}, FF, and η vary from 1% to 4%. R_S increased significantly by ≈12% for the DH weathering. The differences in changes in the electrical parameter between UV exposure and DH exposure can be explained by diverging aging characteristics.
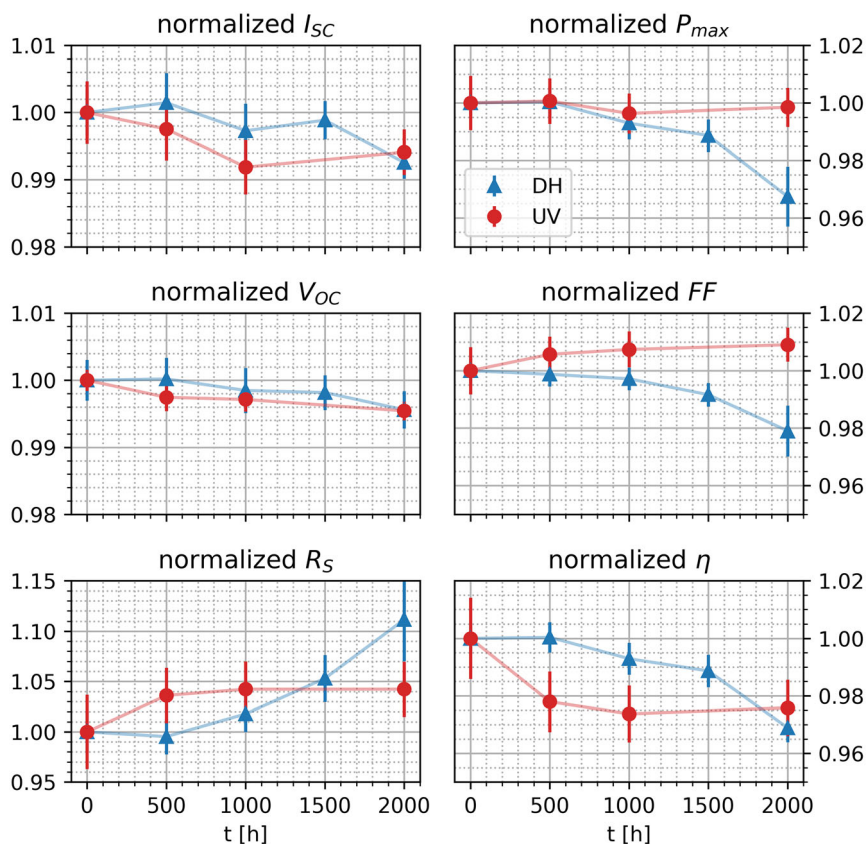

Figure 1. Electrical parameters of mini-modules under DH weathering (blue) and UV weathering (red) in dependence on the weathering time.

Considering the I_{SC} measurements, the UV weathering caused a higher degradation rate than the DH weathering. Within this work, the same encapsulant as in one of our previous weathering cycles was used.[24] Comparing the UV spectrum of the weathering chamber (see Figure S8, Supporting Information) with the previous weathering, especially the intensity of the 300–350 nm interval is less harmful for the UV aging carried out within this work. The previously weathered samples did not show changes in the optical properties determined by UV/VIS measurements and also the formed C=C bonds (which can lead to discoloration) occur only after 1750 h.[24] Thus, as the UV-aged modules of this work did not show browning and the degradation already started within 500 h, the decrease of I_{SC} is probably caused by the degradation of the passivation layer of the solar cell.[20,33,34] This is also in accordance with the constant V_{OC} decrease which is reported in the literature for the degradation of the passivation layer as well as the formation of defects in the bulk of PERC solar cells.[20,33–35] Witteck et al. reported that photons with wavelengths smaller than 353 nm may break Si—H bonds which leads to increased surface recombination.[33] As the used EVA (see Section 2.1) is also transmitting photons in that wavelength interval, the effect may also occur here. The small I_{SC} increase after 2000 h of weathering is most likely a result of deviations between the different sample batches and should not be over-interpreted as a general trend for the other weathering steps observed. However, the electrical parameters at the maximum power point stayed approximately constant for the UV weathering (not shown within this work), hence the minimal decrease of the P_{max} is most likely a result of the minor increase of the series resistance. Consequently, as P_{max} stays approximately constant while V_{OC} and I_{SC} are decreasing, the FF is increasing. As I_{SC} and V_{OC} decrease, but R_S increases, this is directly reflected in a reduction in efficiency of $\approx 2.25\%$ after 2000 h of weathering.

In contrast to UV weathering, the data of the DH conditions indicate that the aging effects are probably not caused by the degradation of the passivation layer of the solar cell. While there is also a constant decrease of the I_{SC} and the V_{OC}, these changes are less pronounced as for the UV weathering. However, the P_{max} starts to decrease significantly after 1000 h of weathering which is probably caused by the simultaneously increasing R_S. Because I_{SC} and V_{OC} are only minimally decreasing while P_{max} is decreasing more severely, the FF is decreasing by $\approx 2\%$ after 2000 h of weathering. After 2000 h, the R_S increased by $\approx 11\%$ resulting in a η and P_{max} decrease of 3.5%. This R_S increase is probably caused by the corrosion of the solar cell contacts forced by a reaction with acetic acid.[22,36,37] The latter is either a result of the Norrish Type II reactions or hydrolysis of the EVA.[38–41] In both cases, this will lead to deacetylation of the acetate group. Thus, the deacetylation can be forced by high energy photons, elevated temperature, or/and the presence of water, and can be additionally catalyzed by the formed acetic acid.[42] In addition, further moisture ingress could act as a solvent and thus disperse the acetic acid which brings it to other reaction sites. This explains why the initial R_S increase is higher for the UV-weathered samples while forming a plateau after ≈ 500 h. The UV irradiance is splitting the acetate groups faster (Norrish Type II reaction), however, only a specific amount of moisture is present within the module and no additional moisture is diffusing inside due to the dry weathering conditions which prevents the autocatalytic reaction. In contrast, the hydrolysis-based process takes place more slowly at the beginning under DH conditions but does not slow down due to the constant penetration of moisture and its autocatalytic reaction.

This assumption is confirmed by the EL measurements displayed in **Figure 2**. For the UV weathering, no EL decrease was detected within 2000 h of weathering. For DH weathering, in contrast, the deacetylation starts slower, but the diffused-in moisture results in a constant R_S increase and a decrease of EL.[37] The water is two-dimensionally penetrating through the backsheet and migrating around the solar cell afterward while reacting with the electrical contacts.[43,44] Although the process of EL reduction starting from the edges of the module toward the center is described many times in the literature,[45,46] the exact cause of this path is still unclear. However, it is obvious
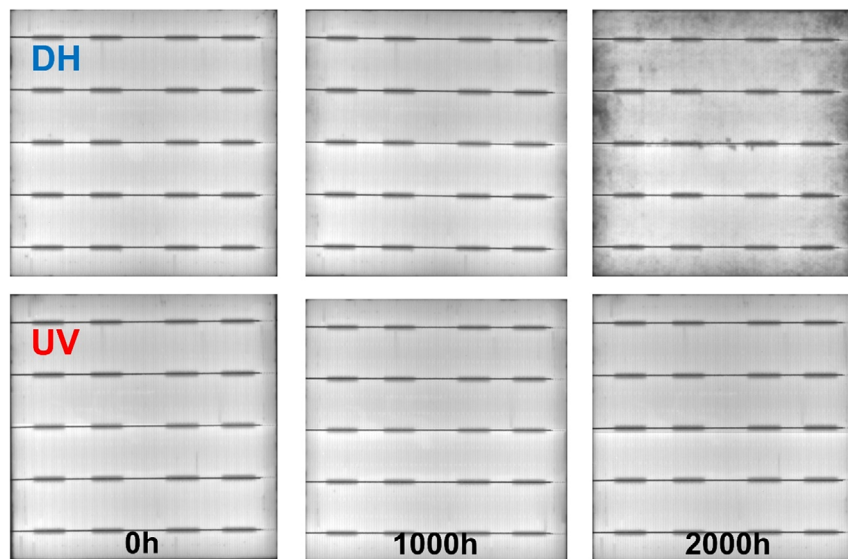

Figure 2. EL measurements of mini-modules under DH weathering (top, blue) and UV weathering (bottom, red) in dependence on the weathering time.

that the moisture penetrating from the rear at these points only has a short path to the top of the solar cell. The hydrolysis of the EVA then takes place almost simultaneously at the top and bottom of the edge area of the solar cell, so that the electrical contacts on both sides degrade resulting at the highest increase of R_S at these positions. Although Jankovec et al. have shown that the diffusion path of the moisture runs mainly via the backsheet,[43,44] diffusion from the edges can still be expected in the edge area, which should further intensify the effect.

3.2. EPR Study

HALS is used to delay the photo-oxidative degradation of an EVA encapsulant. These antioxidant additives act by catalytically inactivating free radicals produced by photo-oxidation through a complex mechanism involving nitroxide radical intermediates.[47–49] Being stable organic radicals, a method of choice for studying nitroxides is EPR spectroscopy.

Several species are involved in the mechanism of action of HALS, including stable nitroxide radicals (**Figure 3** and 12). HALS are added to polymers in their amine form (HN—NH). By reaction with radicals generated through photooxidation, amines are activated to nitroxide form ($^{\bullet}$ON—NH), which in reaction with a carbon-centered radical based on EVA fragments graft to it in the form of alkoxyamine (EVA-ON—NH). The same sequence of reactions can occur on the other amine moiety of HALS.[50]

In all analyzed samples, we observed a multiline EPR spectrum of nitroxide radicals which contains an unpaired electron spin $S = \frac{1}{2}$ (Figure 5 and S1, Supporting Information). The overall shape, characterized by three-hyperfine lines, is dominated by the hyperfine interaction of the electron spin with the nuclear spin $I = 1$ of the ^{14}N nucleus. The EPR spectrum exhibits another typical feature of nitroxide radicals with reduced mobility: line broadening, especially of the high field line. It is well known that the EPR spectrum of nitroxides is highly dependent on their molecular mobility.[51] When in liquid solution, highly mobile nitroxides exhibit a symmetrical three-line EPR signal. In the solid state, depending on the degree of freedom, the appearance of the nitroxide radical EPR spectrum can vary.[52]

EasySpin package for MATLAB and a homemade program developed for such simulations have been used to quantify this motion. Considering an anisotropic rotational correlation time
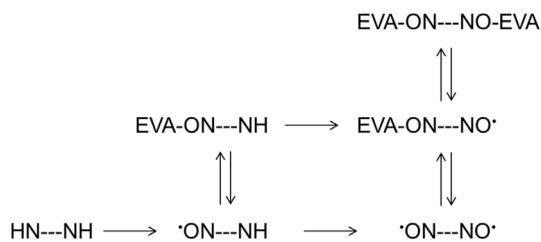
t_{corr}, with a long $t_{corr} = 14$ ns along x, a short $t_{corr} = 0.5$ ns along y, and an intermediate $t_{corr} = 2$ ns along z directions, the main features of the experimental signal are well reproduced (**Figure 4**). This result indicates that in its nitroxide form, HALS undergoes a slow motion in a quasi-rigid limit. While the appearance of EPR spectra of nitroxide HALS intermediates usually does not evolve over the course of polymer aging, their concentration may change, indicating HALS transformation. In a typical case of polymer aging, nitroxide radical intermediate accumulates in the initial phase of photooxidation, then peaks, and finally decreases as HALS are transformed into other forms.[53] The rate of peaking depends on the severity of oxidative conditions: harsher conditions (high temperature, intense light, presence of oxygen) cause nitroxide form to peak sooner.[54] Although HALS are still active as antioxidants in their grafted, alkoxylamine form (EVA-ON—NO-EVA), chemical degradation of the polymer accelerates only once the nitroxide intermediate has peaked, decreased, and stabilized at a low concentration.[55]

The set of samples analyzed by EPR spectroscopy consisted of four timepoints (0, 500, 1000, and 2000 h) for two aging conditions previously described (DH and UV), and two sampling positions for each: the center of the mini-module and the edge of the mini-module (Figure 7). For UV samples, it was observed that the concentration of nitroxides increases for both edge and center positions until 1000 h, when it peaks at the edges, but continues to increase in the center. Since the experiment was stopped at 2000 h, nitroxide concentration peaking in the center was not reached (**Figure 5**). In contrast, a different behavior is observed for DH conditions. The detected concentrations of nitroxide radicals are lower at both positions and for all timepoints, as compared to UV conditions. An increase in nitroxide concentration is observed until 1000 h for both positions, after which it seems to stagnate. Since DH conditions consisted of exposing mini modules only to high temperature and humidity without light irradiation, it is not surprising that HALS are not following the reaction scheme established for classical photooxidation conditions, which was observed for UV conditions. It is possible that the equilibria are shifted toward nonradical species of the Denisov cycle (Figure 3 and 12). Just as under
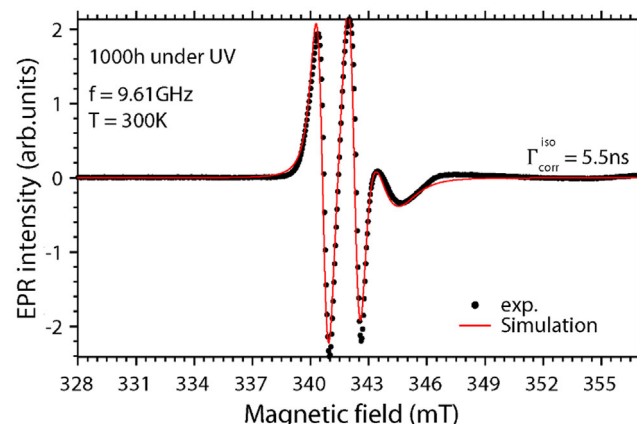
EVA-ON---NO-EVA

$\Updownarrow$

EVA-ON---NH $\longrightarrow$ EVA-ON---NO$^{\bullet}$

$\Updownarrow$ $\Updownarrow$

HN---NH $\longrightarrow$ $^{\bullet}$ON---NH $\longrightarrow$ $^{\bullet}$ON---NO$^{\bullet}$

Figure 3. A schematic representation of chemical transformation of HALS during EVA aging. Only the functional groups of HALS (Tinuvin 770 UV stabilizer) are shown. They are introduced in their amine form (HN—NH) and get transformed to nitroxides on one ($^{\bullet}$ON—NH) or both sides ($^{\bullet}$ON—NO$^{\bullet}$) or alkoxyamines bound to the polymer (EVA-ON—NO$^{\bullet}$ and EVA-ON—NO-EVA).

Figure 4. Experimental X-band cw-EPR spectrum of a sample taken from the edge of the mini-module after 1000 h of aging under "UV" conditions (black dots) and simulated spectrum (red line).
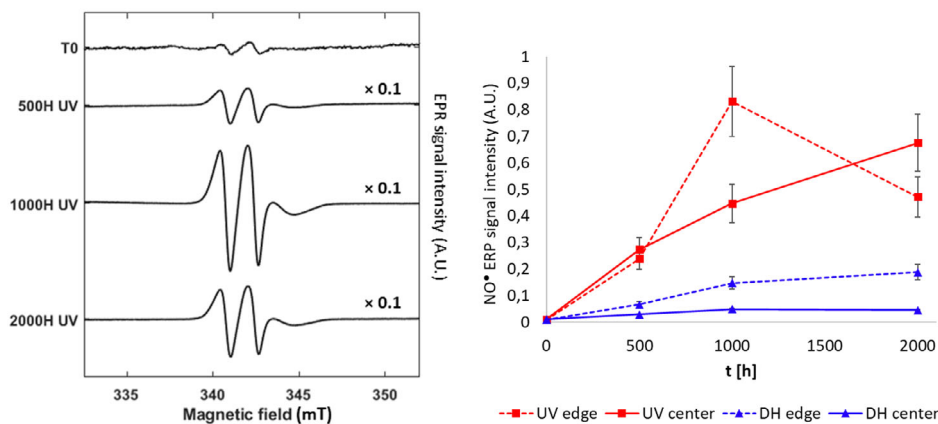
Figure 5. Left: EPR spectra of samples taken from the edge of the mini-module aged under "UV" conditions. EPR spectra of the full set can be found in Supporting Information (Figure S1). Right: graphical representation of nitroxide signal intensity measured by EPR in the entire set of samples.

UV conditions, a higher concentration of nitroxide radical was detected on the edge of the mini-module compared to its center. Differences in the level of exposure of EVA to oxygen and moisture are probably the cause of the differences in aging rate between the edge and center of the mini-module. Two effects may play roles here. The first is that oxygen and water diffuse toward EVA from the sides, affecting only outer several millimeters of EVA. The second is that oxygen and water diffuse through backsheet equally at all positions, but only on the edges affecting both layers of EVA, since in the center solar cells act as a barrier preventing exposure of the front EVA layer (Figure 7). More detailed information about the spatial distribution of nitroxides throughout the mini-modules was provided by EPR imaging.

EPR imaging experiment was performed on a sample taken from the mini-module aged during 1000 h, as it showed the highest difference in concentrations of nitroxide between edge and center. This experiment allows 2D mapping of the nitroxide radical within the sample, while the third spatial dimension (thickness of the mini-module) is averaged. In **Figure 6**, part C, we can observe that the concentration of nitroxide radical is higher toward the edge of the mini-module, and that it drops toward the center. More precisely, the concentration of nitroxide is low on the very edge of the mini-module since it was covered with a protective aluminum foil that blocked UV rays, and thus protected the EVA layer. The peak of the nitroxide radical concentration is found in the region of the mini-module in between the part protected by aluminum foil and the segment which contains silicon photovoltaic cells (the region in **Figure 7** indicated by dashed red arrow). While the aluminum foil protected both EVA layers from UV light, the front EVA layer of the center region was protected from oxygen and water diffusion through the backsheet by silicon cells that acted as a barrier. At the spot where the concentration of nitroxide peaked, EVA was exposed both to UV light and to oxygen and water diffusing through backsheet, which resulted in a higher rate of aging.

Spectral/spatial EPR imaging (Figure S3 and S4, Supporting Information) confirmed that the only observed paramagnetic species are nitroxide radicals.

3.3. Orbitrap MS

To characterize the difference of both aging conditions at the molecular level, encapsulants at the edge of the mini modules were analyzed by Orbitrap MS. Indeed, as it was demonstrated by EL and EPR analyses, the most variations were obtained at the edge compared to the center. In addition, sampling on the edge of the mini-module avoids the presence of silicon particles in the solutions after solvent extraction, which is preferable to avoid dirtying the instrument.

The mass spectrum obtained by APCI(+)-Orbitrap for the native mini-module is displayed in **Figure 8**. The mass spectra of samples after both UV and DH aging are presented in Figure S6, Supporting Information. The major signals obtained for each mass spectrum correspond to the protonated HALS $[C_{28}H_{52}N_2O_4 + H]^+$. Logically, this signal decreases progressively with both types of aging. It underlines that the HALS is consumed or is no longer found in its native form during aging. For the native sample, signals from EVA encapsulant can be observed below the HALS with Gaussian distributions between m/z 200 and 1000 as it can be observed in the enlargement in Figure 8. It is important to note that intact EVA polymers should be found at much higher masses that could not have been detected in the current mass range. The molecules that are observed in this study result from the extraction in n-heptane with ultrasonic bath, which probably allowed to solubilize small size chains or to fragment larger mass chains which then become detectable in the investigated mass range. Major ions of this Gaussian distribution correspond to hydrocarbon molecules (HC) with characteristic mass differences of CH_2 units corresponding to 14.01565 Da. Other EVA molecules with up to 4 VA units are observed below these HC major distributions. It is then assumed that the HC molecules correspond to the EVA polymer termination unit, or to several ethylene repeats that have solubilized in heptane using the current protocol. Finally, these compounds are used as reference for the native polymer signal. Interestingly, in the most aged samples (DH-2000 h and UV-2000 h), these distributions change in appearance, as the major hydrocarbon signals are no longer separated by
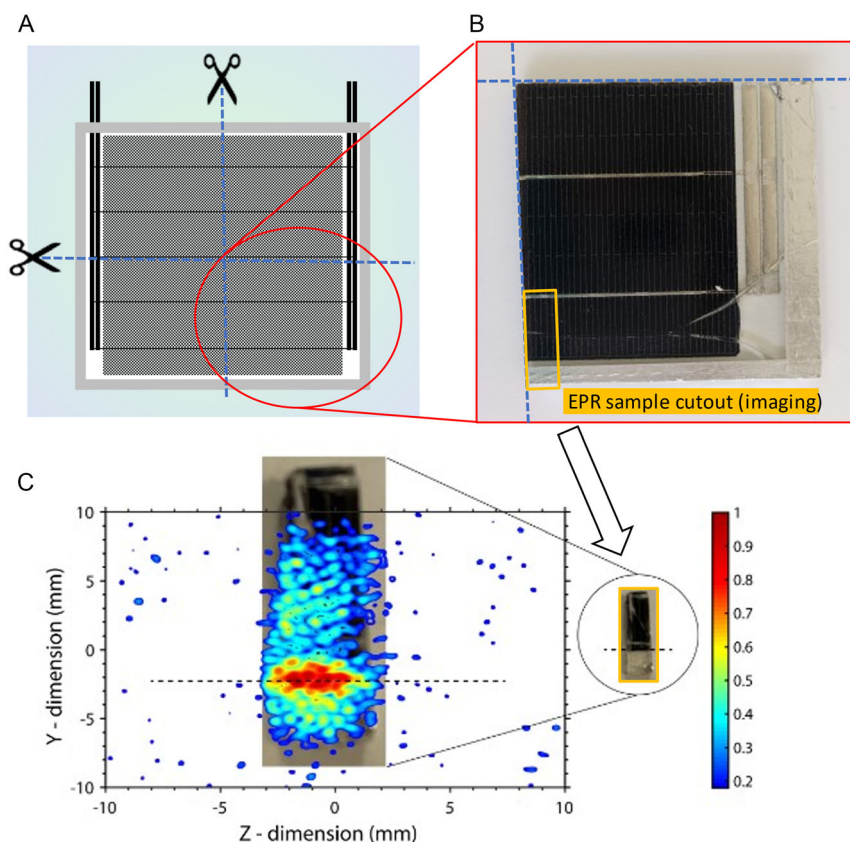
Figure 6. A) Schematic representation of the mini-module with indications of sampling for EPR spectroscopy. B) A quarter of the mini-module after 1000 h of aging under "UV" conditions with indication of the cutout of the sample for EPR imaging. C) EPR imaging: 2D map of the spatial distribution of nitroxide radical within a cutout piece of the mini-module (5.0×20 mm). The relative abundance of nitroxide radicals is presented as a color scale. The results were confirmed on a different sample (results presented in Supporting Information, Figure S2).
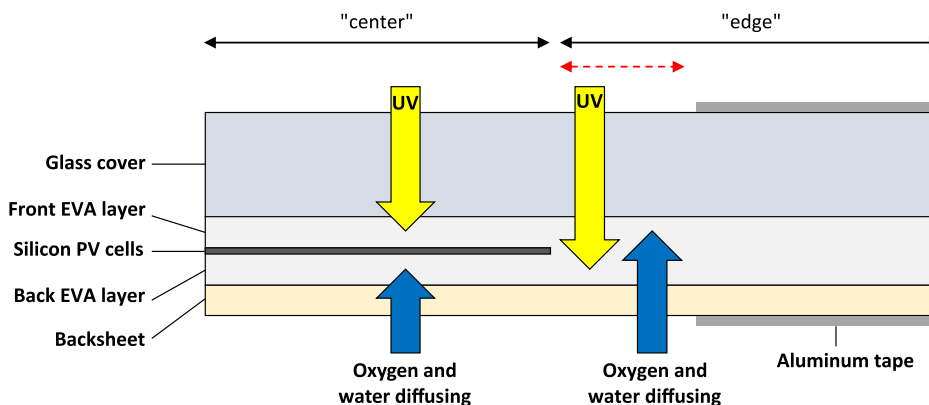

Figure 7. A cross-section of the PV module where we see both "edge" and "center" regions. We can observe that in the center region, the front EVA layer is only under the effect of UV, while the back layer is only under the effect of oxygen and water diffusing through the backsheet. The portion of "edge" region indicated by red arrow is influenced by both.

CH_2 mass differences, but by C_5H_8 gaps. Thus, it means that one additional unsaturation is obtained for each C_5H_8 unit. Such mass differences can be explained by the loss of the acetate group (and the corresponding formation of acetic acid) from the vinyl acetate unit during aging. Indeed, deacetylation of EVA is widely described in the literature through Norrish II reactions or hydrolysis.[38,56,57] This evidences that EVA was subjected to chemical modification with aging, with probable fragmentation of polymer
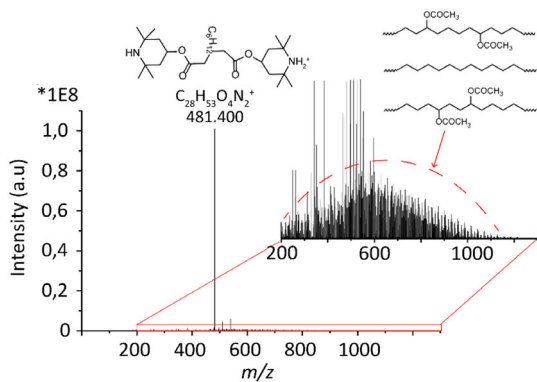
Figure 8. APCI(+)-Orbitrap mass spectrum obtained for the native mini-module sample, with its corresponding enlargement.

chains which were detached from the polymer network and then solubilized during the extraction process.

3.3.1. Focus on EVA Encapsulant

Double bond equivalent versus carbon number maps (DBE vs C#) are used to characterize this modification of encapsulant at the molecular level. To focus on the encapsulant, the major compound class HC is considered in **Figure 9** for the native and the different aging durations. O_1 and O_2 compound classes are also displayed in Figure S7, Supporting Information. These both compound classes are in a minority compared to the HC compound class, but they can also provide information on the polymer's state of degradation, particularly regarding oxidation. As described below (see **Figure 10**), these molecules do not correspond to complete EVA molecules but to small chains that were solubilized with the extraction process. For the native

sample, molecules are observed between C10 and C70 with DBE values below 5. Significant differences are obtained after aging, regardless of the type of aging. Indeed, after aging, the distributions of HC, O_1, and O_2 compounds display molecules with higher DBE values up to 15 with both aging times. Major compounds after aging are separated by the C_5H_8 unit as discussed below (see Figure 10). For instance, distributions of HC compound class are almost identical between DH-2000 h and UV-2000 h, which underlines that the degradation of EVA occurs mainly by a loss of acetic acid on the vinyl acetate functions. It should be noted that the presence of O_1 and O_2 compounds could be coherent with Norrish III reaction forming ketones. Comparing both types of aging, it is interesting to note that these polyunsaturated markers are less abundant for UV-500 h and UV-1000 h. Indeed, for these two aging durations, major molecules are the same as those observed in the native sample. This trend is not observed for DH aging in which polyunsaturated markers are the most abundant molecules from DH-500 h. Although degradation of an EVA polymer seems to occur through deacetylation, these results highlight differences in aging kinetics with these two types of aging.

These aging kinetics are examined in detail with chemical class distributions in Figure 10. For DH and UV aging, the native HALS (O_4N_2) decreases from 60% to almost 10% of the relative natural abundance with UV and DH at 2000 h, underlining that it is consumed regardless of the aging conditions. Concerning the HC compound class, which mainly corresponds to the EVA degradation signals, the increase corresponds to the formation of the polyunsaturated markers through the deacetylation described above (Norrish II). The increase in relative abundance of this class is significantly greater in the DH (up to 65%) than in the UV (up to 45%). Concerning oxygen-containing compounds, it can be noticed that compound classes with more than 3 oxygen atoms only decrease in relative abundance with both types of aging. Furthermore, oxygen addition is not the major path of
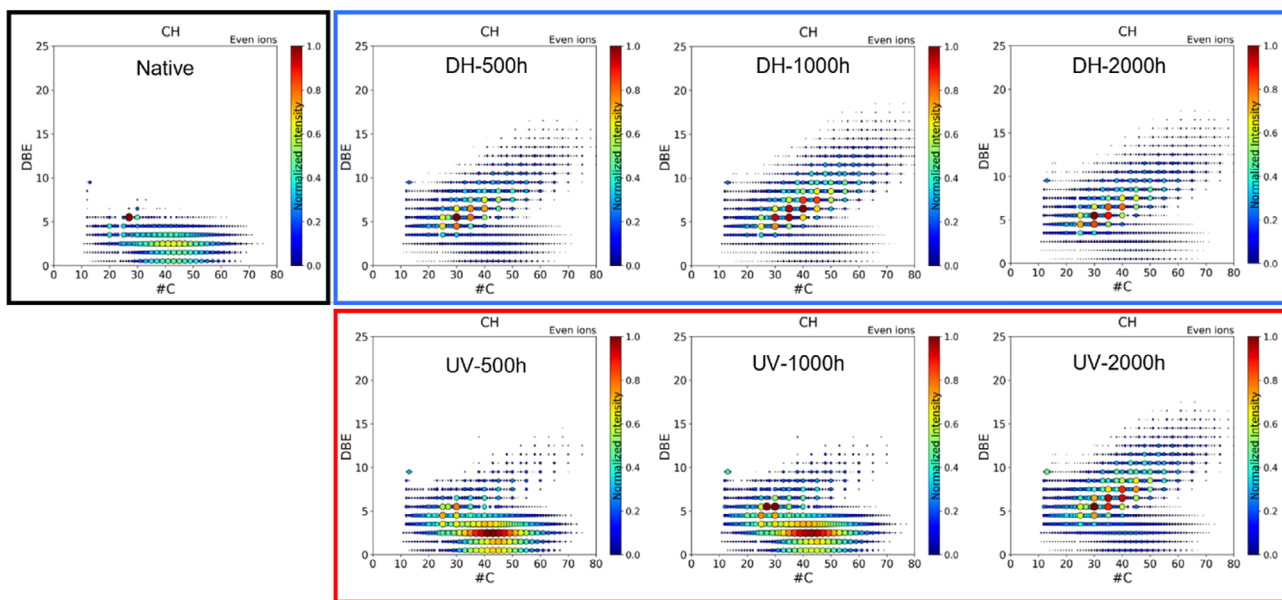

Figure 9. DBE versus C# maps of the HC compound class were obtained for the different mini-module samples.
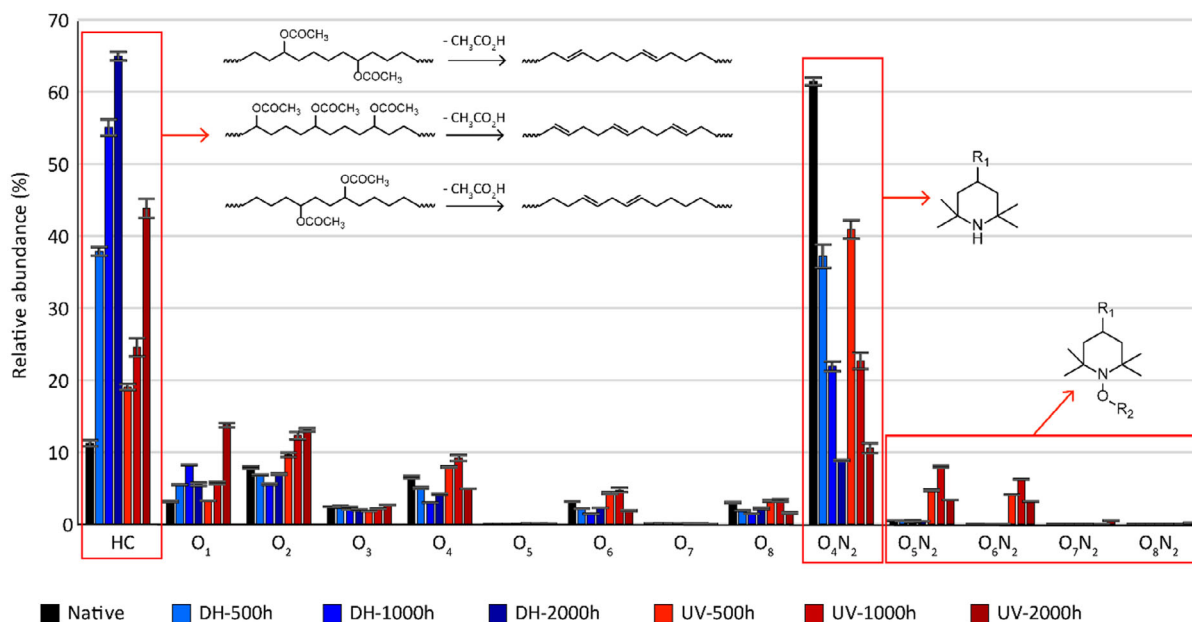
Figure 10. Compound class distributions were obtained with APCI(+)-Orbitrap data for the native and aged samples. Error bars are obtained from standard deviation calculated with the analytical triplicate. For the structure of HALS molecule, R_1 corresponds to the rest of the HALS molecule ($C_{19}H_{34}O_4N$) and R_2 group corresponds to an EVA degradation product.

EVA degradation. The O_4, O_6, and O_8 compound classes correspond to EVA molecules including 2,3, and 4 EVA units, respectively. These compound classes decreased with aging which further proves deacetylation as the major polymer degradation pathway. Only O_1 and O_2 compound classes increase in relative abundance with aging, especially in UV aging, which seems coherent with the formation of ketones or aldehydes (Norrish III). However, these classes are still in the minority compared to the HC class. Interestingly, the occurrence of N_2O_{5-8} compound classes is observed in UV aging while they are not detected in the DH aging. Both N_2O_5 and N_2O_6 compound classes first occurred at UV-500 h, increased in relative abundance at UV-1000 h, and then decreased between UV-1000 h and UV-2000 h with the occurrence of N_2O_{7-8}. This could be correlated with the lower increase in EVA degradation products at UV-500 h and UV-1000 h compared to DH.

To investigate the difference between UV and DH aging, KMD plots representing all the data of each sample are plotted in **Figure 11**. These diagram uses are based on CH2 units to represent homologous compounds varying only by CH_2 addition on horizontal lines. KMD plots are widely used to represent polymer data obtained by mass spectrometry.[58–62] As annotated in Figure 11, the major compound obtained for each sample corresponds to the HALS, and this compound decreases significantly in relative abundance with aging for both DH and UV conditions. The N_2O_X compound classes can easily be observed for UV aging using this representation. These compounds seem to correspond to the interaction product between nitroxide from HALS and a piece of EVA degradation product. These products are then probably obtained by the trapping mechanism of HALS as it was described with the Denisov cycle (EVA-ON—NH). This suggests that the trapping mechanism of HALS did not occur in DH

conditions. By correlating these observations with those obtained with the DBE versus C# maps focused on EVA degradation products, it can be assumed that the HALS reduced the EVA degradation in UV conditions, especially at UV-500 h and UV-1000 h of aging, as only a few EVA degradation products are observed. However, a decrease in the HALS efficiency seems to be observed from UV-2000 h as O_5N_2 and O_6N_2 compound classes decreased in relative abundance, and as the EVA degradation products significantly increased in relative abundance. As DH aging does not display any of these products, it evidences that the HALS does not work the same way in the presence of moisture. As the EVA degradation products are observed in significant abundance from the first point of aging at DH-500 h, it can be supposed that the HALS is deactivated in the presence of moisture or the absence of UV irradiation, preventing the trapping mechanism of HALS.

4. Summary of the Results and Discussion

In this study, three analytical techniques to investigate the aging of solar modules under DH and UV weathering conditions have been used. Macroscopically, the modules have been analyzed with $I–V$ characterization and EL measurements. On the molecular level, the encapsulant (i.e., the EVA polymer and the HALS additive) was analyzed by EPR and orbitrap mass spectrometry. The results indicate a difference in the aging behavior of the solar modules under different weathering conditions as well as topological variations in the aging rate within the modules. The electrical performance decrease of the solar modules is related to the degradation of the passivation layer and the degradation of the encapsulant which leads to the corrosion of the electrical
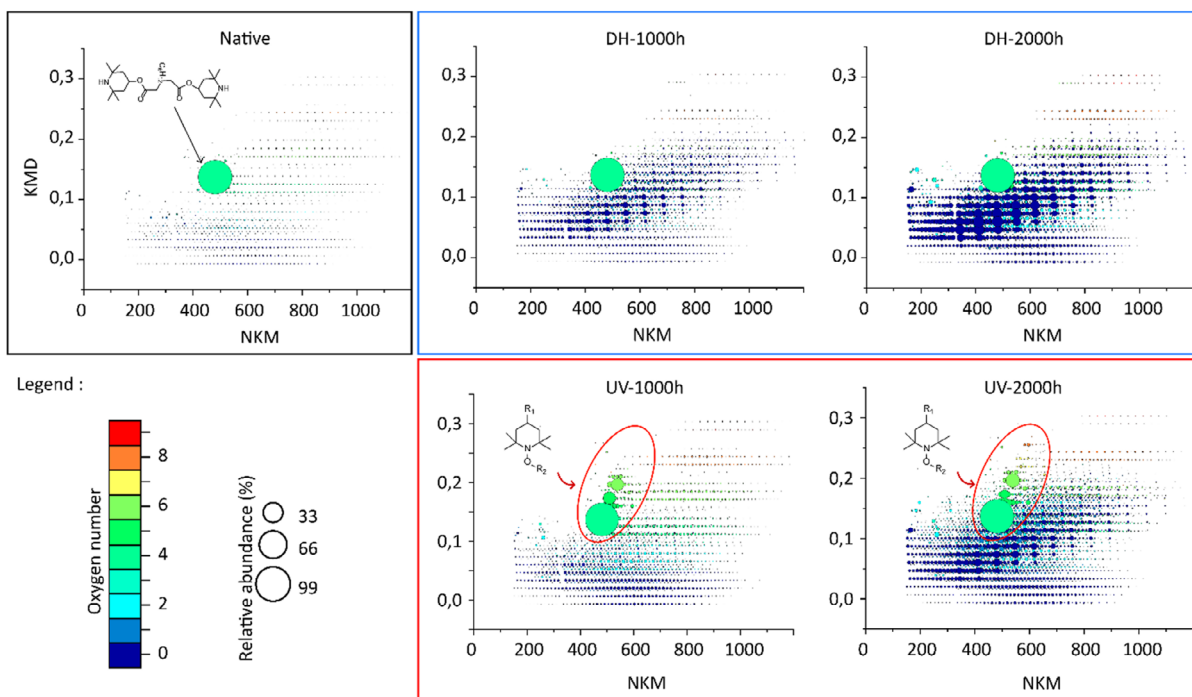
Figure 11. KMD plot obtained with APCI(+)-Orbitrap data for the native and aged samples. For the structure of HALS molecule, R_1 corresponds to the rest of the HALS molecule ($C_{19}H_{34}O_4N$) and R_2 group corresponds to an EVA degradation product.
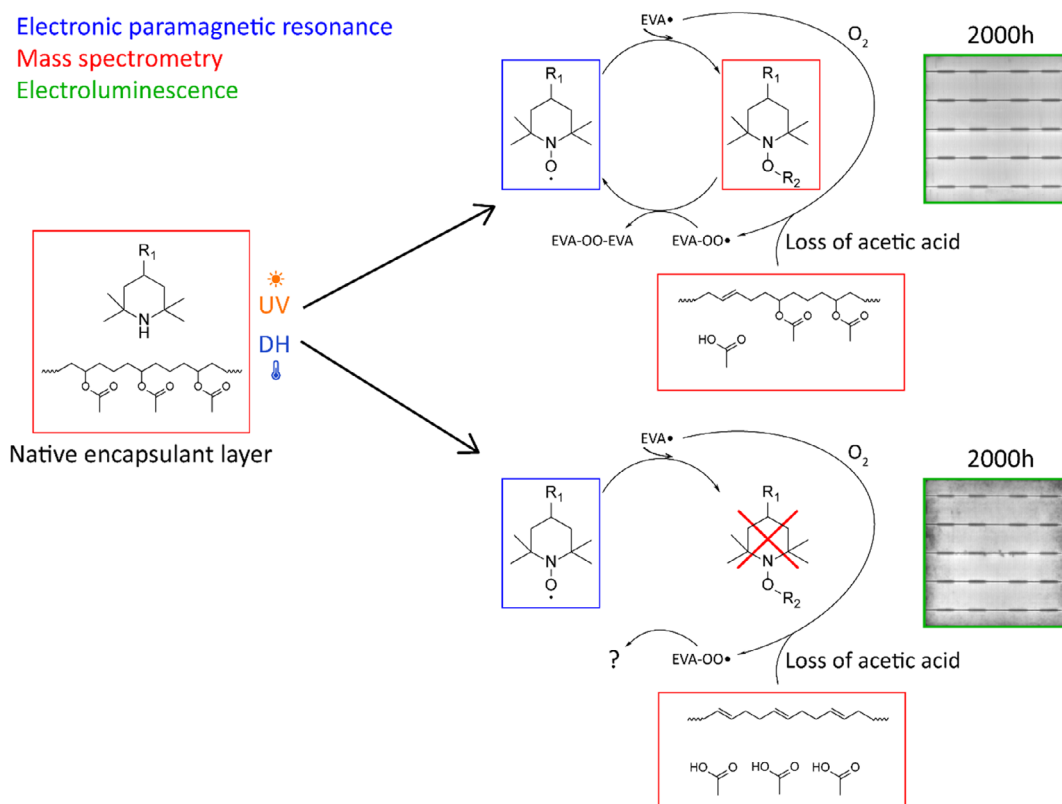

Figure 12. Summary diagram of the different results obtained with each technique for the two aging types. For the structure of HALS molecule, R_1 corresponds to the rest of the HALS molecule ($C_{19}H_{34}O_4N$), and R_2 group corresponds to an EVA degradation product.

contacts. Changes in short circuit current, maximum power output, open circuit voltage, fill factor, efficiency, and series resistance of the mini-modules exposed to UV and DH weathering were studied. UV weathering caused degradation of the passivation layer of the solar cell, while DH weathering caused a more severe degradation of the encapsulant resulting in the release of acetic acid and more pronounced contact damage (see Figure 1). EL measurements confirmed the difference in the degradation mechanisms between the two weathering conditions. It also indicated topological differences in the rate of performance loss, which was more pronounced at the edges (see Figure 2). This result was confirmed by the EPR analysis. For both aging conditions, a higher concentration of nitroxide was detected at the edges of the mini modules as compared to the center (see Figure 5 and 6), indicating faster aging at the edges.

Orbitrap mass spectrometry covers a wide range of molecular descriptors as it is displayed in **Figure 12**. Orbitrap results indicate that HALS native amine form is consumed at approximately equal rates for both weathering types. In reaction with free radicals of the autoxidation process, HALS are initially converted to stable nitroxide radicals ($^\bullet$ON—NH) (see Figure 3). Quantification of nitroxide radicals by EPR spectroscopy showed that their concentration was lower in DH than in UV samples for all respective aging time points. This result suggested that HALS was engaged in different mechanisms in the two weathering conditions. Further transformation of HALS involves the reaction of nitroxide radical with a carbon-centered radical originating from autoxidation processes to yield alkoxyamine (EVA-ON---NH). Orbitrap mass spectrometry results confirmed the difference in the HALS functioning in the two aging conditions: polymer-grafted alkoxyamine intermediate was detected only in UV samples, suggesting uncommon HALS activity under DH conditions (see Figure 11 and 12). The common case of HALS activity with nitroxide peaking was detected at the edge of the mini-module under UV conditions (see Figure 5).[53]

Concerning EVA, degradation seemed to occur mainly through deacetylation for both aging conditions. However, the reason for the deacetylation is different. For UV weathering, this is caused by high-energy photons and Norrish-type reactions.[38,39] For DH weathering, the EVA is subject to hydrolysis.[40,41] Previous studies suggested that the autocatalytic deacetylation of EVA was responsible for the strong acetic acid formation, the discoloration of the encapsulants, and therefore also for the degradation of solar modules by corroding the electrical contacts.[36,63,64] Similar molecular distributions of polyunsaturated products of deacetylation were detected in both aging conditions by Orbitrap MS (see Figure 9).

However, a comparison of the relative abundance of these markers of deacetylation revealed their higher presence in DH samples (see Figure 10). Higher rates of deacetylation resulted in higher production of acetic acid that corroded contacts, and thus increased R_S and lowered P_{max} in DH samples (see Figure 1). EVA degradation under DH conditions seems to be autocatalytically hydrolysis driven[40,42] under realistic environmental conditions, in conjunction with radiation which generates more radicals,[24,28,39] this can lead to an increased degradation rate of the modules. Furthermore, moisture is probably required for the distribution of acetic acid in dry climates. If this is not the case, deacetylation itself has only minor effects on the module performance, as it was seen for the modules after UV weathering.

5. Conclusion

Although the separation of the vinyl acetate group could be confirmed as the main cause of EVA degradation for UV and DH weathering, the reasons and consequences for the respective solar modules are very different. Radicals created by photodegradation can be bound by the UV stabilizer under UV weathering and the effect on the encapsulant is only minimal. Minor reductions in the electrical parameters for this type of weathering result from the degradation of the cell or the passivation layers. However, the study carried out has shown that the UV stabilizer is hindered in its mechanism of action under DH weathering. Due to the lack of stabilization, the EVA could have strongly degraded under DH weathering by hydrolysis, although the energy introduced by the chamber temperature is significantly lower than photon energy from the UV range. The resulting acetic acid formation has subsequently led to corrosion of the contact fingers and thus to significant performance losses.

These findings can have far-reaching consequences for modules in the field. In very few climates can only one type of stressor be expected. This work and various literature sources have shown that additive-based stabilization of EVA is essential to ensure resistance to environmental influences. Consequently, further studies should investigate how antioxidants and amine-based stabilizers behave under combined stress conditions within the encapsulant in solar modules. Furthermore, hydrolysis of EVA is a serious problem for the lifetime of solar modules, the addition of hydrolysis-stabilizing additives in encapsulants should be considered. The microclimates created within such a module (e.g., by the diffusion of moisture) require a successive analysis of all components to understand the degradation behavior of the compound.

Conflict of Interest

The authors declare no conflict of interest.

Data Availability Statement

The data that support the findings of this study are available from the corresponding author upon reasonable request.

[1] F. J. M. M. Nijsse, J.-F. Mercure, N. Ameli, F. Larosa, S. Kothari, J. Rickman, P. Vercoulen, H. Pollitt, *Nat. Commun.* **2023**, *14*, 6542.

[2] M. Aghaei, A. Fairbrother, A. Gok, S. Ahmad, S. Kazim, K. Lobato, G. Oreski, A. Reinders, J. Schmitz, M. Theelen, P. Yilmaz, J. Kettle, *Renewable Sustainable Energy Rev.* **2022**, *159*, 112160.

[3] D. C. Jordan, N. Haegel, T. M. Barnes, *Prog. Energy* **2022**, *4*, 022002.

[4] L. Koester, S. Lindig, A. Louwen, A. Astigarraga, G. Manzolini, D. Moser, *Renewable Sustainable Energy Rev.* **2022**, *165*, 112616.

[5] G. Oreski, J. S. Stein, G. C. Eder, K. Berger, L. Bruckman, R. French, J. Vedde, K. A. Weiß, *Prog. Energy* **2022**, *4*, 032003.

[6] M. Tao, V. Fthenakis, B. Ebin, B. Steenari, E. Butler, P. Sinha, R. Corkish, K. Wambach, E. S. Simon, *Prog. Photovoltaics* **2020**, *28*, 1077.

[7] M. Halwachs, L. Neumaier, N. Vollert, L. Maul, S. Dimitriadis, Y. Voronko, G. C. Eder, A. Omazic, W. Mühleisen, Ch Hirschl, M. Schwark, K. A. Berger, R. Ebner, *Renewable Energy* **2019**, *139*, 1040.

[8] A. Omazic, G. Oreski, M. Halwachs, G. C. Eder, C. Hirschl, L. Neumaier, G. Pinter, M. Erceg, *Sol. Energy Mater. Sol. Cells* **2019**, *192*, 123.

[9] B. Brune, I. Ortner, G. C. Eder, Y. Voronko, G. Oreski, K. A. Berger, K. Knöbl, L. Neumaier, M. Feichtner, *Prog. Photovoltaics* **2023**, *31*, 716.

[10] R. Heidrich, M. Lüdemann, A. Mordvinkin, R. Gottschalg, *IEEE J. Photovoltaics* January **2024**, *14*, 131.

[11] A. P. Patel, A. Sinha, G. Tamizhmani, *IEEE J. Photovoltaics* **2020**, *10*, 607.

[12] R. Heidrich, A. Mordvinkin, R. Gottschalg, in *2023 IEEE 50th Photovoltaic Specialists Conf. (PVSC)*, San Juan, PR, USA June **2023**, pp. 1–3.

[13] F. Prieto-Castrillo, N. Núñez, M. Vázquez, *Prog. Photovoltaics* **2020**, *28*, 1308.

[14] I. Kaaya, J. Ascencio-Vásquez, K.-A. Weiss, M. Topič, *Sol. Energy* **2021**, *218*, 354.

[15] A. Bala Subramaniyan, R. Pan, J. Kuitche, G. TamizhMani, *IEEE J. Photovoltaics* **2018**, *8*, 1289.

[16] IEC TS 62788-7-2, *Measurement Procedures for Materials used in Photovoltaic Modules - Part 7-2: Environmental Exposures - Accelerated Weathering Tests of Polymeric Materials*, International Electrotechnical Commission, Geneva, Switzerland **2017**.

[17] Terrestrial Photovoltaic (PV), *Modules – Design Qualification and Type Approval – Part 2: Test Procedures*, Vol. *IEC 61215-2:2021*, International Electrotechnical Committee, Geneva, Switzerland **2021**.

[18] K. Hara, *J. Photochem. Photobiol. A* **2022**, *425*, 113721.

[19] C. Peike, T. Kaltenbach, K.-A. Weiß, M. Koehl, *Sol. Energy Mater. Sol. Cells* **2011**, *95*, 1686.

[20] J. Lindroos, H. Savin, *Sol. Energy Mater. Sol. Cells* **2016**, *147*, 115.

[21] R. Asadpour, X. Sun, M. A. Alam, *IEEE J. Photovoltaics* **2019**, *9*, 759.

[22] A. Kraft, L. Labusch, T. Ensslen, I. Durr, J. Bartsch, M. Glatthaar, S. Glunz, H. Reinecke, *IEEE J. Photovoltaics* **2015**, *5*, 736.

[23] C. Barretta, G. Oreski, S. Feldbacher, K. Resch-Fauster, R. Pantani, *Polymers* **2021**, *13*, 271.

[24] R. Heidrich, C. Barretta, A. Mordvinkin, G. Pinter, G. Oreski, R. Gottschalg, *Sol. Energy Mater. Sol. Cells* **2024**, *266*, 112674.

[25] F. Pern, *Sol. Energy Mater. Sol. Cells* **1996**, *41–42*, 587.

[26] M. C. C. de Oliveira, A. S. A. Diniz Cardoso, M. M. Viana, V. de F. C. Lins, *Renewable Sustainable Energy Rev.* **2018**, *81*, 2299.

[27] M. Çopuroğlu, M. Şen, *Polym. Adv. Tech.* **2004**, *15*, 393.

[28] P. Klemchuk, M. Ezrin, G. Lavigne, W. Holley, J. Galica, S. Agro, *Polym. Degrad. Stab.* **1997**, *55*, 347.

[29] A. Jentsch, K.-J. Eichhorn, B. Voit, *Polym. Test.* **2015**, *44*, 242.

[30] R. Heidrich, A. Mordvinkin, R. Gottschalg, *Polym. Test.* **2023**, *118*, 107913.

[31] S. Stoll, A. Schweiger, *J. Magn. Reson.* **2006**, *178*, 42.

[32] M. Sueur, J. F. Maillard, O. Lacroix-Andrivet, C. P. Rüger, P. Giusti, H. Lavanant, C. Afonso, *J. Am. Soc. Mass Spectrom.* **2023**, *34*, 617.

[33] R. Witteck, B. Veith-Wolf, H. Schulte-Huxel, A. Morlier, M. R. Vogt, M. Köntges, R. Brendel, *Prog. Photovolt: Res. Appl.* **2017**, *25*, 409.

[34] V. Guiheneuf, F. Delaleux, S. Pouliquen, O. Riou, P.-O. Logerais, J.-F. Durastanti, *Sol. Energy* **2017**, *157*, 477.

[35] F. Ye, Y. Li, W. Deng, H. Chen, G. Liao, Z. Feng, N. Yuan, J. Ding, *Sol. Energy* **2018**, *170*, 1009.

[36] M. D. Kempe, G. J. Jorgensen, K. M. Terwilliger, T. J. McMahon, C. E. Kennedy, T. T. Borek, *Sol. Energy Mater. Sol. Cells* **2007**, *91*, 315.

[37] C. Peike, S. Hoffmann, P. Hülsmann, B. Thaidigsmann, K. A. Weiβ, M. Koehl, P. Bentz, *Sol. Energy Mater. Sol. Cells* **2013**, *116*, 49.

[38] F. J. Pern, *Angew. Makromol. Chem.* **1997**, *252*, 195.

[39] J. Jin, S. Chen, J. Zhang, *Polym. Degrad. Stab.* **2010**, *95*, 725.

[40] M. Patel, S. Pitts, P. Beavis, M. Robinson, P. Morrell, N. Khan, I. Khan, N. Pockett, S. Letant, G. Von White, A. Labouriau, *Polym. Test.* **2013**, *32*, 785.

[41] K. Hara, Y. Chiba, *J. Photochem. Photobiol. A* **2021**, *404*, 112891.

[42] B. Sultan, E. Sörvik, *J. Appl. Polym. Sci.* **1991**, *43*, 1737.

[43] M. Jankovec, F. Galliano, E. Annigoni, H. Y. Li, F. Sculati-Meillaud, L.-E. Perret-Aebi, C. Ballif, M. Topic, *IEEE J. Photovoltaics* **2016**, *6*, 1152.

[44] M. Jankovec, S. Mitterhofer, J. Slapsak, M. Topic, in *2020 47th IEEE Photovoltaic Specialists Conf. (PVSC)*, IEEE, Calgary, AB, Canada **2020**, pp. 1308–1312.

[45] M. Koehl, S. Hoffmann, S. Wiesmeier, *Prog. Photovoltaics Res. Appl.* **2017**, *25*, 175.

[46] J. Zhu, M. Koehl, S. Hoffmann, K. A. Berger, S. Zamini, I. Bennett, E. Gerritsen, P. Malbranche, P. Pugliatti, A. Di Stefano, F. Aleo, D. Bertani, F. Paletta, F. Roca, G. Graditi, M. Pellegrino, O. Zubillaga, F. J. C. Iranzo, A. Pozza, T. Sample, R. Gottschalg, *Prog. Photovoltaics Res. Appl.* **2016**, *24*, 1346.

[47] J. L. Hodgson, M. L. Coote, *Macromolecules* **2010**, *43*, 4573.

[48] S. Commereuc, S. Scheirs, V. Verney, J. Lacoste, *J. Appl. Polym. Sci.* **1998**, *69*, 1107.

[49] S. Commereuc, P. Lajoie, V. Verney, J. Lacoste, *Polym. Int.* **2003**, *52*, 576.

[50] K. A. Harrison, E. A. Haidasz, M. Griesser, D. A. Pratt, *Chem. Sci.* **2018**, *9*, 6068.

[51] E. Bordignon, in *eMagRes* (Eds: R. K. Harris, Wasylishen, R. L.)), John Wiley & Sons, Ltd, Chichester, UK **2017**, pp. 235–254.

[52] E. Etienne, A. Pierro, K. C. Tamburrini, A. Bonucci, E. Mileo, M. Martinho, V. Belle, *Molecules* **2023**, *28*, 1348.

[53] J. L. Gerlock, D. F. Mielewski, D. R. Bauer, *Polym. Degrad. Stab.* **1989**, *26*, 241.

[54] J. L. Gerlock, D. R. Bauer, L. M. Briggs, *Polym. Degrad. Stab.* **1986**, *14*, 53.

[55] J. Durmis, D. J. Carlsson, K. H. Chan, D. M. Wiles, *J. Polym. Sci. B Polym. Lett. Ed.* **1981**, *19*, 549.

[56] S. Jiang, K. Wang, H. Zhang, Y. Ding, Q. Yu, *Macro React. Eng.* **2015**, *9*, 522.

[57] B. K. Sharma, U. Desai, A. Singh, A. Singh, *J. Appl. Polym. Sci.* **2020**, *137*, 48268.

[58] H. Sato, S. Nakamura, K. Teramoto, T. Sato, *J. Am. Soc. Mass Spectrom.* **2014**, *25*, 1346.

[59] T. Fouquet, S. Nakamura, H. Sato, *Rapid Commun. Mass Spectrom.* **2016**, *30*, 973.

[60] T. Fouquet, H. Sato, *Mass Spectrom.* **2017**, *6*, A0055.

[61] T. N. J. Fouquet, R. B. Cody, Y. Ozeki, S. Kitagawa, H. Ohtani, H. Sato, *J. Am. Soc. Mass Spectrom.* **2018**, *29*, 1611.

[62] O. Lacroix-Andrivet, C. Castilla, C. Rüger, M. Hubert-Roux, A. L. Mendes Siqueira, P. Giusti, C. Afonso, *Energy Fuels* **2021**, *35*, 2165.

[63] A. W. Czanderna, F. J. Pern, *Sol. Energy Mater. Sol. Cells* **1996**, *43*, 101.

[64] G. A. Razuvaev, B. B. Troitskii, L. V. Chochlova, Z. B. Dubova, *J. Polym. Sci. B Polym. Lett. Ed.* **1973**, *11*, 521.